AGU100 ADVANCING EARTH AND SPACE SCIENCE

JGR Atmospheres

RESEARCH ARTICLE
10.1029/2019JD030449

Key Points:
- A spatial-temporal extreme precipitation event (EPE) database is generated from high-resolution IMERG data
- The database allows analyses of many event-based precipitation characteristics that conventional data sets are unable to provide
- Results from CONUS show spatial/seasonal distributions of EPEs, as well as many other characteristics over different seasons

Correspondence to:
Y. Zhou,
yaping.zhou-1@nasa.gov

Citation:
Zhou, Y., Nelson, K., Mohr, K. I., Huffman, G. J., Levy, R., & Grecu, M. (2019). A spatial-temporal extreme precipitation database from GPM IMERG. *Journal of Geophysical Research: Atmospheres*, *124*, 10,344–10,363. https://doi.org/10.1029/2019JD030449

Received 11 FEB 2019
Accepted 20 JUL 2019
Accepted article online 30 AUG 2019
Published online 15 OCT 2019

Author Contributions:
Conceptualization: Yaping Zhou, Karen I. Mohr, Robert Levy
Formal analysis: Yaping Zhou, Kevin Nelson
Investigation: Yaping Zhou
Methodology: Yaping Zhou, Karen I. Mohr, Mircea Grecu
Resources: Mircea Grecu
Software: Yaping Zhou, Kevin Nelson
Visualization: Kevin Nelson
Writing - original draft: Yaping Zhou
Writing – review & editing: Yaping Zhou, Kevin Nelson, Karen I. Mohr, George J. Huffman, Robert Levy

A Spatial-Temporal Extreme Precipitation Database from GPM IMERG

Yaping Zhou[1,2], Kevin Nelson[3], Karen I. Mohr[4], George J. Huffman[5], Robert Levy[1], and Mircea Grecu[5,2]

[1]Climate and Radiation Laboratory, NASA-Goddard Space Flight Center, Greenbelt, MD, USA, [2]Goddard Earth Sciences Technology and Research, Morgan State University, Baltimore, MD, USA, [3]Department of Physical and Environmental Sciences, Texas A&M University-Corpus Christi, Corpus Christi, TX, USA, [4]Earth Sciences Division-Atmospheres, NASA-Goddard Space Flight Center, Greenbelt, MD, USA, [5]Mesoscale Atmospheric Processes Laboratory, NASA-Goddard Space Flight Center, Greenbelt, MD, USA

Abstract Extreme precipitation events (EPEs) have the potential to create catastrophic flooding, landslides, and infrastructure damage. We diagnose the spatial and temporal characteristics of EPEs by using the Integrated Multi-SatellitE Retrievals for Global Precipitation Measurement mission (GPM; IMERG) precipitation estimates to construct spatial-temporal (*xy-t*) EPEs that depict both the spatial extent and temporal evolution of precipitation systems. EPEs were constructed using a recursive-fractal approach to classify the precipitating grids across space and time as belonging to the same system, thus identifying events. This classification enables the accurate depiction of duration, areal coverage, total volume, and propagation of each EPE over its entire life cycle. Results from 4 years of IMERG statistics over the contiguous United States show that the most frequent EPEs have duration between 3 and 6 hr, an affected area of 10^3–5×10^4 km^2, and a total precipitation volume of 10^6–10^8 m^3. Spatially, EPEs occur most frequently in the northwest and northeast in the winter and spring and the southwest and southeast in summer. Fall has the least number of EPEs, and summer exhibits some of the heaviest and largest precipitation events. The diurnal cycle in frequency and precipitation volume is most prominent in summer, weaker in spring and fall, and is not discernible in winter, especially for events lasting fewer than 6 hr. The event propagation speeds indicate the influence of large-scale circulations as winter events tend to move faster than those in the other seasons.

1. Introduction

Extreme precipitation events (EPE) are one of the leading causes of natural hazards to human lives and society, as they can lead to major flooding, soil erosion, and landslides. Observational and modeling studies in recent years have shown an overall increased risk of extreme precipitation events in warmer climates (Zwiers & Kharin, 1998; Hegerl et al., 2004; Groisman et al., 2005; Allan & Soden, 2008; O'Gorman & Schneider, 2009; Min et al., 2011; Lau et al., 2013; Greve et al., 2014; Kendon et al., 2014; Donat et al., 2016; Taylor et al., 2017; and many others).

Traditionally, extreme precipitation is defined by computing the maximum precipitation or precipitation above a given threshold in a set of fixed durations (i.e., 1- or 5-days). Such a threshold of extreme precipitation can be defined globally or locally as a fixed precipitation amount, percentile, or recurrence interval, that is, return period. International working groups on extreme events have proposed 10 indices for extreme precipitation, including annual maximum 1- and 5-day precipitation, number of heavy (>10 mm/day) and very heavy (>20 mm/day) days, annual total precipitation from top 95% and 99% days, and maximum consecutive wet days (Donat et al., 2013; Zhang et al., 2011). While all of these precipitation indicators capture important aspects of the precipitation characteristics, they do not cover all aspects of EPEs. Daily resolution precipitation indicators will not capture the duration and maximum intensity of subdaily precipitation events. The spatial scale of regionally heavy precipitation cannot be represented by any grid-based precipitation indices, as the traditional method of analysis of grid-based precipitation data sets with fixed spatial and temporal resolution tends to treat precipitation in each grid box and time interval as an isolated event, or a snapshot, rather than an evolving, propagating event.

This study leverages the expanded information content of newer data sets and describes a fractal-based methodology to understand precipitation characteristics that cannot be extracted from older data sets and methodologies. The duration, spatial extent, and speed of storm propagation contribute to the local and regional precipitation accumulation and affect the impact of heavy precipitation events. These characteristics have been difficult or impossible to extract from older, lower-resolution gridded data sets.

The stakes for understanding duration, extent, and propagation of EPEs are high. Climate change studies suggest that extreme precipitation will become more intense and of shorter duration as the climate warms (Haerter et al., 2010; Kendon et al., 2014; Prein et al., 2017; Utsumi et al., 2011). With increasing local temperature, the temporal distribution of extreme precipitation within a storm could have a narrower peak, potentially leading to more flash flooding (Wasko & Sharma, 2015; Westra et al., 2014). Weaker tropical circulation leading to slower moving systems could also increase the precipitation recycling rate and the total accumulation for a given location (Dwyer & O'Gorman, 2017; Kossin, 2018). Meanwhile, Taylor et al. (2017) found intensification of mesoscale convective system (MCS) in the West Africa Sahel since 1982 due to increased meridional temperature gradient and wind shear. An improved understanding of extreme precipitation in the current climate, its variability, and controlling mechanisms will benefit future climate projection efforts.

As many of the EPEs have temporal scales of only a few hours, it is evident that temporally high-resolution (e.g., half-hourly or shorter) precipitation observations are necessary to characterize extreme precipitation and detect any small changes, especially for subdaily events leading to flash flooding. Previously, station- or grid-based precipitation duration has been computed to describe the persistence or longevity of the system at a given station or grid (Dairaku et al., 2004; Trenberth et al., 2017; Wu et al., 2018). A multiday system will usually produce more total precipitation for a specific location. However, multiday precipitation systems usually move with a transient synoptic weather system in middle- and high-latitudes and tropical waves, meaning that Eulerian grid-based duration statistics do not capture the true longevity of the system.

Precipitation system sizes have been studied extensively with connected satellite imagery (Mohr et al., 1999; Nesbitt et al., 2006; Liu, 2011). A useful example is the precipitation feature (PF) database generated by the University of Utah/Texas A&M-Corpus Christi (Liu et al., 2008; Liu & Zipser, 2015). The PFs are constructed based on continuous precipitating pixels from the Tropical Rainfall Measuring Mission (TRMM) Precipitation Radar and TRMM Microwave Imager during the TRMM era (Liu et al., 2008), and the Global Precipitation Measurement mission (GPM) Dual Polarization Radar and GPM Microwave Imager more recently (Liu & Zipser, 2015). Each PF is a snapshot of the cloud and precipitation system that, when combined with other snapshots from different systems, can be accumulated to create statistics about system life cycles. Life cycles measured in binned mean size/volume of PF labeled by time of day provide some insights on how precipitation systems vary diurnally (Liu & Zipser, 2008; Nesbitt & Zipser, 2003; Zhou et al., 2013).

To consider precipitation events as a moving system with a spatial scale, Dwyer and O'Gorman (2017) constructed precipitation events from climate model simulations with a duration and a zonal length. They find that the speed of zonal movement of a heavy precipitation center is correlated well with zonal wind speed at 600 mb. However, since their methodologies only consider the zonal direction, their measure of length cannot represent a true spatial scale or the total volume of precipitation systems, which display a variety of complex spatial structures. Midlatitude squall lines are rarely oriented purely zonally or meridionally, and their propagation may vary from the geostrophic zonal wind (Trenberth & Zhang, 2018). Thus, a spatial extent accounting for both zonal and meridional directions over time is essential to capture the full spatial scale and propagation of a precipitation system.

An object-oriented approach of defining precipitation events has emerged in recent years, in which precipitation events are defined with statistical tracking methods (Chang et al., 2016; Davis et al., 2006; Skok et al., 2009, 2010, 2013). A similar cloud-tracking algorithm is used to track tropical convection (Dias et al., 2012). Using an algorithm developed by Skok et al. (2009), White et al. (2017) tracked heavy rainfall events (>24 mm/day) in space and time, using 3-hourly TRMM data from 40°N–40°S with a focus on rainfall duration. Ren et al. (2012) developed an algorithm to track regional heavy precipitation system using station data. These algorithms expect the precipitation or cloud field to be continuous in space and/or time, meaning that a noncontinuous (but still organized) system may not be interpreted correctly. The fine structure of heavy regional precipitation would be missed.

The U.S. GPM Science Team produces an Integrated Multi-satellitE Retrievals for GPM (IMERG) at a 0.1° × 0.1°, 30-min resolution (Huffman et al., 2018). This data set builds on the legacy of the TRMM Multisatellite Precipitation Analysis at 3-hourly, 0.25° × 0.25° resolution and 50°S–50°N coverage (Huffman et al., 2010). The IMERG algorithm merges precipitation estimates from an international constellation of passive microwave sensors from low Earth orbit satellites and geosynchronous Earth orbit infrared sensors. The research version of IMERG incorporates precipitation gauge analyses to provide crucial regionalization and bias correction to the satellite estimates. The IMERG product provides a unique opportunity to study the systematic dependence of precipitation frequency and intensity at a higher temporal and spatial resolution than previous precipitation products. The IMERG data set also allows for the construction of extreme events with two spatial dimensions plus a time dimension that can be used to study the life cycle, impact area, depth, and many other characteristics of EPEs not previously accessible from older data sets.

Section 2 describes the algorithm for constructing EPEs from IMERG and some case studies. Section 3 presents statistical results in association with various properties of EPEs over the contiguous United States (CONUS). A brief summary and discussion are provided in section 3.

2. Constructing Precipitation Events From IMERG

2.1. Algorithm Description

Developing the EPE algorithm begins with defining what constitutes an EPE. Events with prolonged intense precipitation and covering a large area that could lead to major flooding and disaster, such as those associated with tropical cyclones and monsoon troughs can be considered as EPE. But not all EPEs have to have large temporal or spatial scales. A localized thunderstorm with a heavy downpour over the period of a couple of hours can also be extreme and cause localized flash flooding. In contrast, some synoptic precipitation systems may not be extreme in terms of precipitation intensity but can be extreme in terms of total volume and area coverage. Furthermore, a given rain rate could be moderate in a wet region, but quite extreme in a dry region. Of course, the hydrologic impact of a given rain rate depends on multitude of factors such as soil moisture. But here we only focus on precipitation itself relative to its local climatology. To encompass all these situations, we require that all the EPE events have some locally defined extreme precipitation cells to start with. An EPE could have multiple discontinuous (locally) extreme cells in space and time and light precipitation grids surrounding these cells. Here, we define a local extreme threshold at each grid as (mean +2.5 × stdev) based on raining grids/periods (>0.01 mm/hr) during March 2014 to February 2018 (Figure 1). Over CONUS, every grid has rain only 2–8% of the study period (Figure 1b). Therefore, the mean rain rate for the raining period (Figure 1a) is much higher than the mean rain rate over the entire study period (Figure 1a multiplied by Figure 1b). The extreme threshold (Figure 1c) is generally more than 5 times of the mean rain rate for the raining period, and the number of grids that qualifies as extreme is generally less than 1.5% of all raining grids (Figure 1d), and even lower if all grids are considered (Figure 1d multiplied Figure 1b). This threshold is high enough to exclude moderate rain events, but not events with longer duration or larger size but less intense instantaneous rain rates.

Constructing *xy-t* EPEs is not a trivial task because their multidimensional nature imposes potentially large computer memory requirements. The algorithm must be quick and efficient, as well as avoid loading the entire data set into the memory. The simplest method for grouping precipitating grids into events is to search a region with a given center and a radius. This method works well for circular systems with known centers, such as tropical cyclones (Zhou et al., 2010) and elliptically organized convective systems (Liu & Zipser, 2015) but would be difficult for linearly oriented convective systems such as squall lines because the specified radius could either be too large or too small. Too large a radius will mistakenly lump independent events into the same event, while one that is too small will cut off areas that belong to the same system. In this work, we first group the aforementioned extreme grids into events using a recursive-fractal approach: using precipitation maxima as a starting point, we recursively aggregate the nearby extreme grids into an event until no more grids can be found that meet the specified conditions. We then find the next maxima and organize an event in the same manner as the first event. In this way, the events grow in spatial and temporal directions following their natural shape. Note that "fractal" here refers to the manner of algorithm execution rather than the structure of derived events. The specific algorithm is as follows:

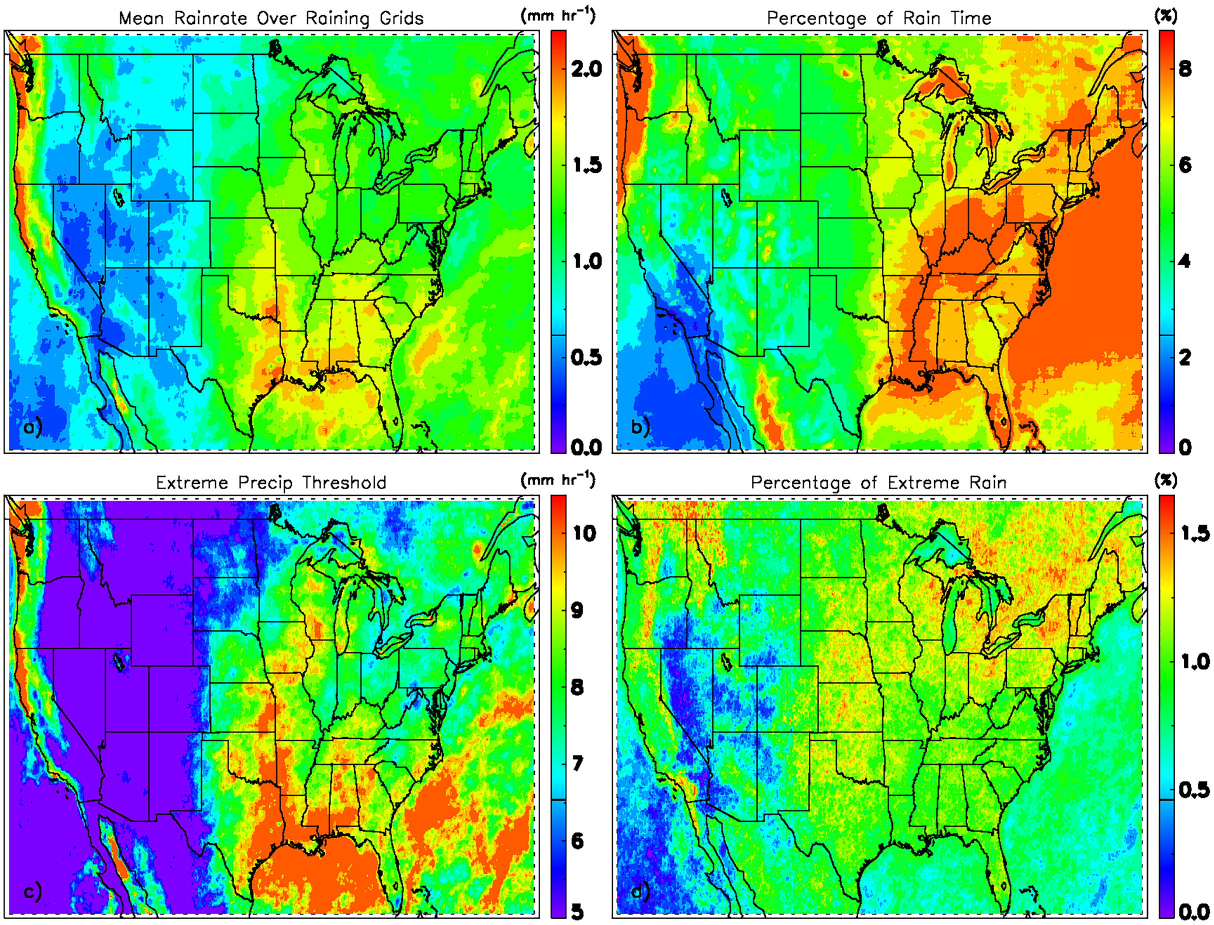

Figure 1. Maps of precipitation for (a) Mean rain rate of raining grids grids (>0.01 mm/hr), (b) Percentage of raining time, (c) Extreme threshold used in this study, and (d) percentage of all grids identified as extreme grids versus all the raining grids. Statistics are based on half-hourly, 0.1° × 0.1° Integrated Multi-SatellitE Retrievals for Global Precipitation Measurement mission data from March 2014 to February 2018.

Assuming R is the precipitation rate at any given instance at grid (x, y), Z, and σ are the mean and standard deviation of the precipitating grid (>0.01 mm/hr) for this grid during the entire period, respectively. R_c is the local extreme precipitation threshold, and r and w are the searching radius and time window from the current precipitating grid, respectively. We use $d_1(t_1)$ and $d_2(t_2)$ as tunable distance (time) intervals for the extreme and light precipitating grids, respectively. The procedure is

1. Define local thresholds $R_c(x,y)$ as

$$R_c(x, y) = Z(x, y) + 2.5\sigma(x, y) \tag{1}$$

In regions where $R_c < 5$ mm/hr, R_c is set to be 5 mm/hr.

2. Find all extreme grids $R > R_c(x,y)$ to form an extreme inventory (EXT).
3. Find the maximum in EXT, that is, $G1(x,y,t)$. Search EXT for any grid ($G2$) that is a neighbor of $G1(r < d_1, w < t_1)$ in the event.
4. Recursively search EXT for the neighboring grids of $G2$, until no more grids can be included in the event. Each time a grid is passed into an event, it is deleted from EXT.
5. For every extreme grid in the event, include nearby light rain ($r < d_2$, $w < t_2$) and $R > 1.0$ mm/hr in the event.
6. Repeat Steps 3–5 until no more grids are left in EXT.
7. Compute statistics of each event.

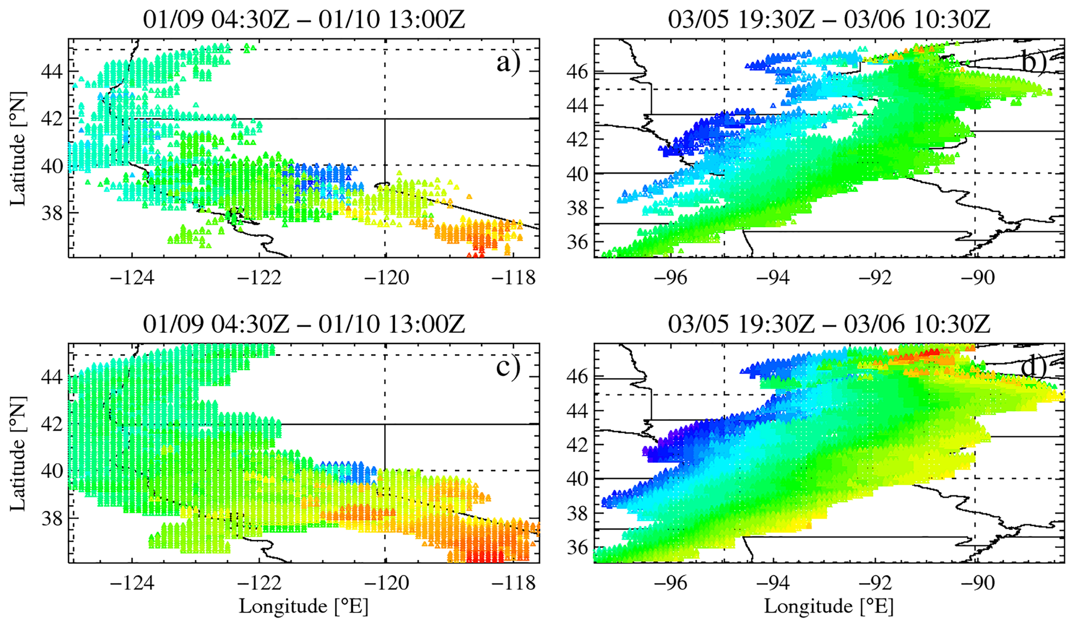

Figure 2. Precipitation grids showing a southeastward propagating winter storm (a and c) for 9–10 January 2017 and an eastward propagating system (b and d) for 5–6 March 2017. The top panels (a and b) only show the grids identified as heavy precipitation; the lower panels (c and d) show both the heavy and the surrounding light rains. The thresholds for heavy precipitation vary by gridded location, as described in the text. The light precipitation has a minimum threshold of 1 mm/hr. Color is evenly distributed across the duration of the events, with blue and red indicating the beginning and ending of the event, respectively.

In the above algorithm, the parameters *r* and *w* allow for some gaps between the precipitation grids, since precipitation is not completely continuous in both space and time. Figure 2 shows the evolution of two EPEs in space, one moving from the northwest to the southeast on the West Coast of the United States on 9–10 January 2017 (Figures 2a and 2c) and another squall-like MCS moving eastward across the Great Plains on 5–6 March 2017 (Figures 2b and 2d). The upper panels, which show the extreme precipitation grids only, are not continuous in space because the algorithm allows gaps between extreme precipitation grids. In the lower panels, lighter precipitation grids fill up most of the gaps between the extreme precipitation grids. The algorithm captures the event evolution in both temporal and spatial directions. Figure 3 provides snapshots of precipitation intensity of the squall line system (Figures 2b and 2d) at the early, peak, and late stages, respectively. The change of intensity and areal coverage during its lifetime, as well as the eastward movement of the system, is captured realistically in these plots.

It is not easy to determine whether two separate precipitation cells belong to the same large system or should be considered as independent systems. In large systems such as tropical cyclones, the distance between rain bands could be over hundreds of kilometers, while independent unit cells have a scale of tens of kilometers. To determine an optimal searching distance and time interval, we conducted sensitivity studies of the EPE identification algorithm during June–August 2017 over CONUS to see how the number of identified events changes with *w* and *r* (Table 1). If the number of extreme events decreases dramatically with slight increases in *w* and *r*, those diminished events could be easily absorbed into nearby events, while truly independent events would remain independent. We observe that the number of events decreases with increasing searching distance and time interval, as expected. However, the rate of decrease in the number of events is not linear. The drop of the number of events from one spatial interval to the next is about 30% for smaller temporal intervals and as low as 6% for longer time intervals. From one temporal interval to next, there is an average of between 12.5% and about 25% decrease in the number of events. The sharpest overall decrease occurs at 90 km and 1.5 hr. Trenberth and Zhang (2018) reported an *e*-folding distance of spatial covariance at about 50 km that could be considered as typical size of the precipitation system in midlatitude continental climate zones. Based on these observations and visual inspection of derived precipitation events, *w* and *r* are set to 50 km and 6 hr for this study. Future work could make these parameters adjustable based on climate regimes and precipitation system morphologies in the area of interest.

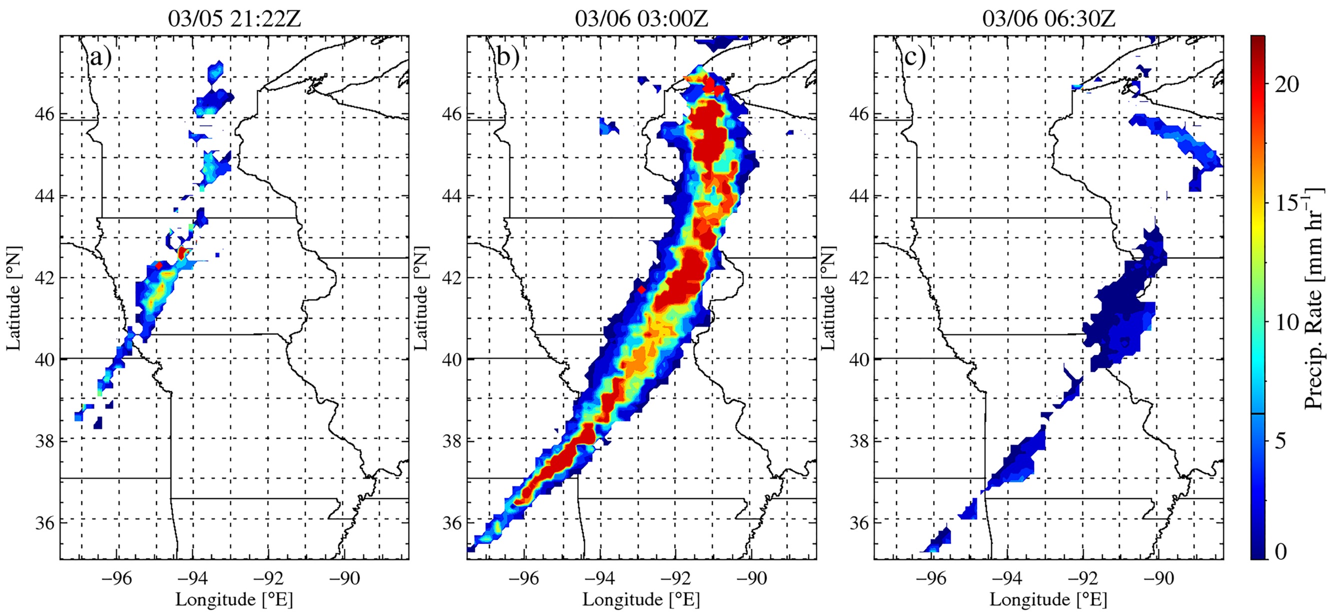

Figure 3. Precipitation fields showing the squall line system (Figures 2b–2d) in the (a) early, (b) mature, and (c) late stage during 5–6 March 2017. Color indicates the precipitation intensity.

As described, the algorithm requires that the entire data record be loaded in the memory for the algorithm to group events in both spatial and temporal domains. Due to the high spatial and temporal resolution of IMERG data, this is extremely challenging. We break the computation down into individual months, which means additional computational methodologies have to be exploited. Because the mean and standard deviation of the entire data set cannot be calculated from monthly mean and standard deviation, a new formulation has to be derived for each quantity (see appendix A). In addition, we require temporal continuity that can merge precipitation events at the end of one month with possible events in the next month.

2.2. Case Studies

As stated in the above section, one of the difficult issues in constructing EPEs is determining whether spatially and temporally separated precipitating grids belong to the same large system. Here we examine two scenarios illustrating the challenges and the overall capability of the algorithm to identify EPEs. One EPE is associated with a hurricane and another with concurrent atmospheric river (AR) events. We selected Hurricane Harvey, which made landfall near Rockport, TX, in August 2017, and a period with a set of active atmospheric river episodes in the coastal North Pacific during winter 2014–2015.

2.2.1. Hurricane Harvey

Harvey started as a typical weak, August tropical storm that affected the Lesser Antilles and dissipated over the central Caribbean Sea. However, after reforming over the Bay of Campeche, Harvey rapidly intensified into a category 4 hurricane on the Saffir-Simpson Hurricane Wind Scale before making landfall along the middle Texas coastal bend. The storm then stalled, with its center over the northern Texas coast near Houston for 4 days, dropping historic amounts of precipitation totaling more than 1,500 mm over southeastern Texas and western Louisiana (Blake & Zelinsky, 2018). Based on Harvey's record, we selected a domain (25°N–35°N, 102°W–87°W) and a period (23–31 August) and then assumed all the precipitation events within this domain and period were associated with Harvey. Ideally, we would hope to identify a single event that included all EPEs from hurricane Harvey rather than splitting into many events. This proved to be difficult. For the algorithm with 50-km/6-hr limits, we found a total of 84 events. The top two events are shown in Figure 4. The first event

Table 1
Number of EPEs Computed From Sensitivity Tests With Different Allowable Distance and Time Intervals Between Precipitating Grids to be Considered in the Same Extreme Event System for Data From JJA 2017

$r\backslash w$ (km)	1.5 hr	3 hr	6 hr	9 hr	12 hr	18 hr
30	17393	14144	11884	10887	10169	8822
50	13121	9631	7484	6620	5972	4757
70	10641	7034	5019	4290	3727	2807
90	8916	5436	3613	2993	2540	1805

Note. Events with single extreme precipitation grid are not included in this calculation.

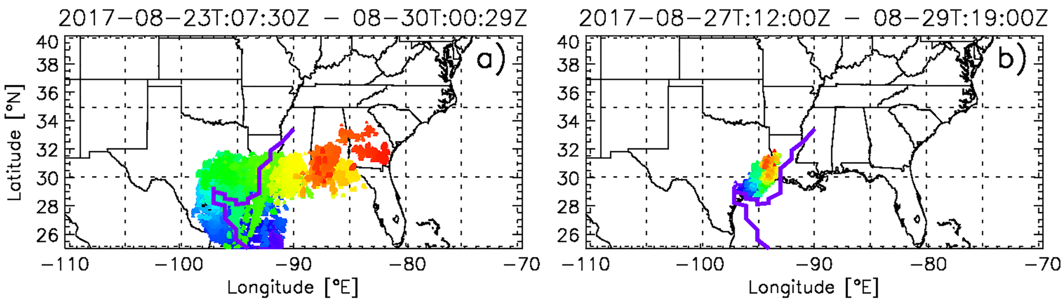

Figure 4. Extreme events associated with hurricane Harvey during 23–30 August 2017. The storm track of Harvey within the domain is shown by the purple line. Color indicates propagation of events as in Figure 2.

(Figure 4a) covers almost the entire period (23–30 August) and captures 89.5% and 77.6% of all extreme and total precipitation from all the EPEs in this period, respectively, while the event in Figure 4b captures 7.8% and 7.3% of extreme and total precipitation, respectively. Together, the top two events capture 97% of the extreme precipitation and 85% of total precipitation from all EPEs during this period (Figure 4). The remainder are small events with total volume less than 0.5% of the volume captured in the main event (Figure 4a).

2.2.2. AR-Related EPEs

Atmospheric rivers are narrow, elongated, synoptic bands of water vapor that play important roles in the global water cycle and regional weather/hydrology. The example in Figure 5 is from winter (December–February, DJF) 2014–2015. The AR trajectory was downloaded from the University of California-Los Angeles AR database developed by Guan and Waliser (2015). The construction of AR events is based on integrated water vapor transport from 6-hourly fields of ERA-Interim reanalysis and the outputs include the AR shape, axis, landfall location, and basic statistics of each detected AR. In Figure 5, we show the top eight extreme events in terms of total volume in the West Coast in the domain (west of 110°W and north of 32°N) with concurrent AR events (axis). We observe that all the major extreme events except one (Figure 5g) have concurrent AR events crossing the region that bring moisture from the Pacific Ocean to the West Coast. Note that many AR regions do not show precipitation in these figures because only one EPE was shown in each figure. The top eight events shown in Figure 5 contain 55.1% and 67.6% of total and extreme precipitation, respectively, of all EPEs in DJF 2015, which corresponds to about 30% of overall precipitation. Here, we have a larger domain and longer time period than for Hurricane Harvey, so there are many smaller events not associated with these major events. This EPE data set will facilitate a more detailed study connecting EPEs with the AR events globally.

3. Results

For each of the events, a range of event parameters can be calculated to characterize the spatial-temporal structure and evolution of the event (Table 2). The parameters include event-oriented characteristics such as event duration, total, or accumulated precipitation volume; total affected precipitation area; accumulated precipitating area; and mean and maximum precipitation depth.

The storm start, peak, and end times provide useful information about the life cycle of precipitation events, especially for subdaily events. The start and end times are the local time computed from the earliest and latest grids of the entire event. Duration is simply the time difference between the latest and earliest grids. Total affected area is computed with all the spatial grids in the event with careful consideration that each grid has multiple precipitation occurrences during the event. Precipitation depth is computed for each grid point in the affected area by summing up all the precipitation received in this grid during the entire event. A maximum and mean depth are computed from all the affected grids. Instantaneous (half-hourly) area coverage and total volume are calculated every half hour during the entire event from the extreme grids and all grids of that time separately so that maximum half-hour rain volume and area can be computed, in addition to maximum extreme-to-total ratio in volume and area, respectively. The time into event when maximum instantaneous volume, area, or extreme-to-total ratio occur are also recorded. The total volume of the event is the sum of all half-hour volumes.

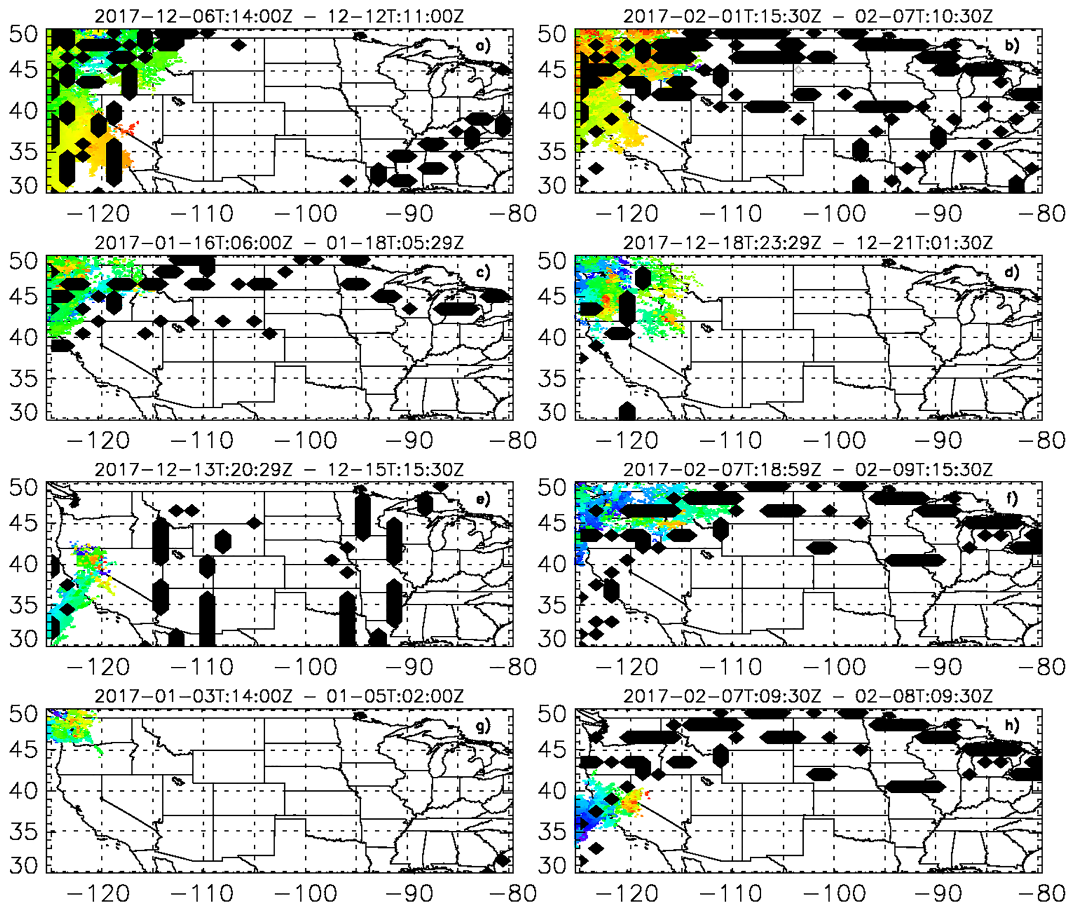

Figure 5. Top eight events by total volume (colored dots with colors indicating propagation of events as in Figure 1) during D2014-JF2015 for the West Coast (center location east of 110°W, north of 32°N) with concurrent atmospheric river (AR) events (black blocks). Note that only one extreme precipitation event is shown in each figure but AR events are not limited to the region. Only one event does not have an AR event in the region. These events correspond to 50% and 65% of total and extreme precipitation in the entire season in the region, respectively.

In addition, we compute the system propagation speed in both zonal and meridional directions by tracking the movement of the center of event at each time step. The event center is defined as average location of all precipitating grids at any instance weighted by precipitation rate. It is usually near the most heavily precipitating grid at any instant.

These parameters provide a comprehensive description of precipitation events, including both their structure and time evolution. Statistics can be derived from these parameters to characterize precipitation events on a

Table 2
Statistical Parameters of Extreme Events

Time	Start, end time of the entire system and period with extreme precipitation.
Location	Center longitude and latitude
Duration	Entire system and period with extreme precipitation
Volume	Entire system and those from extreme and light precipitating grids
Depth	Maximum and mean in precipitation affected area
Areal coverage	Total affected area and maximum instantaneous precipitation area
Intensity	Maximum and mean intensity of the entire system
Extreme-to-total ratio	Maximum instantaneous extreme-to-total ratios in volume and area
Peak time	Time into events when maximum intensity and extreme-to-total ratios occur
Propagation speed	Mean and maximum in horizontal and meridional directions

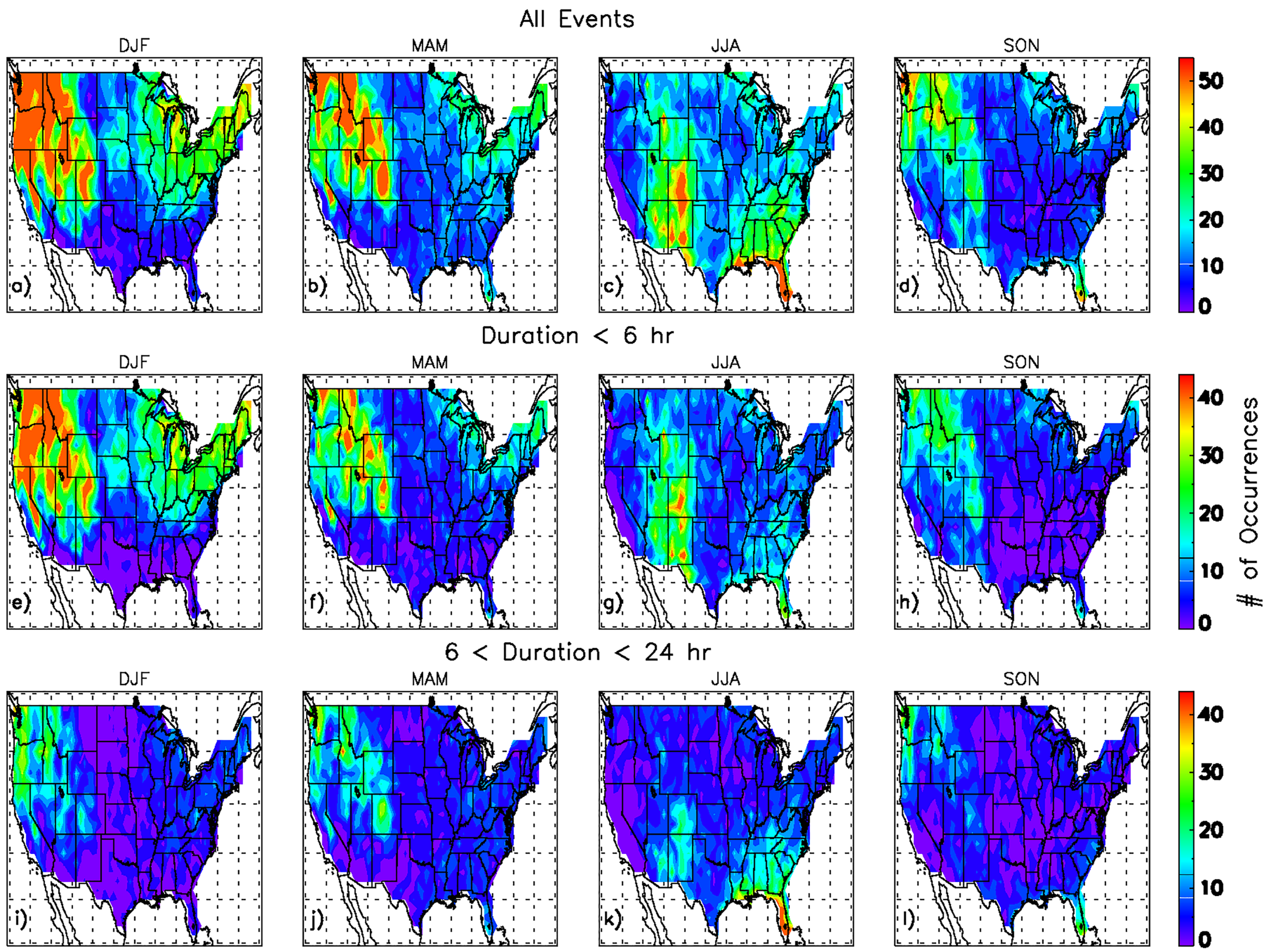

Figure 6. Spatial distribution of rain events for all events (top), duration <6 hr (middle), and 6–24 hr (bottom) in different seasons. DJF = December–February; MAM = March–May; JJA = June–August; SON = September–November.

regional and seasonal basis and to monitor changes in event characteristics over time. In the following sections, we will analyze some of the EPE characteristics over the CONUS domain (25°N–50°N, 125°W–65°W) derived from 4 years of IMERG V05b data (April 2014 to March 2018). In particular, all the histograms are based on events with center locations over CONUS.

3.1. Spatial Distributions of EPEs

The EPEs defined in this study have a wide range of volume, size, and duration. Some have the potential to cause floods and major disasters in a larger area, while others are extreme in a very local and instantaneous context. Here, we show spatial distributions of EPEs for all events (Figures 6a–6d) as well as those with short (<6 hr, Figures 6e–6h) and intermediate (6–24 hr, Figures 6i–6l) durations. Events with significant total volume, affected area, and considerable maximum depth are shown in Figure 7.

In the Pacific Northwest, wintertime (DJF) has the most frequent EPEs due to the southward shift of the upper level jet stream and the low-level transport of moisture from the Pacific Ocean. Orographic enhancement by coastal mountain ranges of the wintertime moist convergent flows can also result in EPEs (Mock, 1996). These events occur at a lower frequency in the spring (March–May, MAM), even less in the fall (September–November, SON), and are largely absent from summer (June–August, JJA). In the northeast, the high frequency of EPEs is usually caused by tropical and extratropical cyclones, the latter storms defined as “nor'easters” (Agel et al., 2015; Kunkel et al., 2012; Pfahl & Wernli, 2012). Nor'easters occur in east coast from October to April, with the most frequent occurrence in January and February. From late spring through

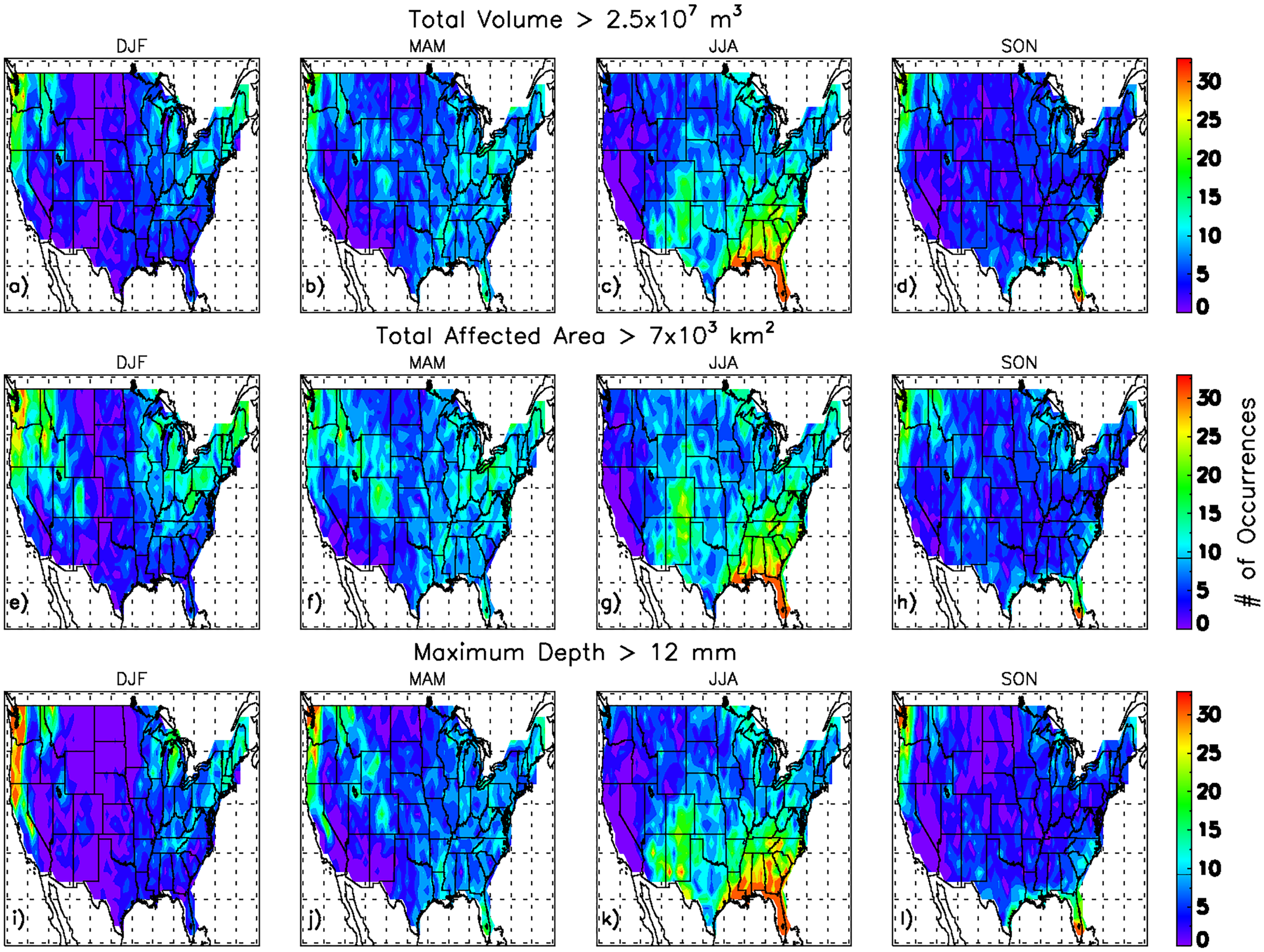

Figure 7. Frequency distributions of events with large total volume (>2.5×10^7 m^3; top), larger affected area (>7×10^3 km^2; middle), and large maximum depth (>12 mm) in each season. DJF = December–February; MAM = March–May; JJA = June–August; SON = September–November.

early fall, MCSs are frequent in this area, sometimes moving from Canada and the Great Lakes region (Agel et al., 2015), and tropical cyclones occur in the summer.

In the southwestern United States, most of the summer precipitation comes from the North American monsoon that starts in July and ends in mid-September (Higgins et al., 1997; Vera et al., 2006). The monsoon moisture from the Gulf of California and the Gulf of Mexico, coupled with local afternoon convection, results in thunderstorms during the season. A swath of high frequency of EPEs can be seen in JJA along the monsoon pathway from the Desert Southwest through the Rocky Mountains. In the southeast United States, EPEs are most frequent in the summer season, when large amounts of moisture from the Gulf of Mexico and Atlantic Ocean intrudes into the coastal states, with occasional tropical cyclones and their remnants spawning EPEs in this region. Most of the EPEs in this region appear as MCSs (Konrad, 1997; Schumacher & Johnson, 2006). The high frequency of EPEs in Florida in JJA is a result of daily thunderstorms that are due to interactions between the large scale (synoptic) wind flow in the lower levels of atmosphere, and the various smaller scale sea, lake, and river breezes in the region (Atkins & Wakimoto, 1997). Figures 6a–6d is consistent with many publications describing the seasonal precipitation variability and system types on the various regions of CONUS. The purpose here is to illustrate how the event identification algorithm produces maps consistent with detailed regional studies often laboriously conducted from station data (Mock, 1996; Vera et al., 2006; Schumacher & Johnson, 2006; Agel et al., 2015, and others)

The frequency distributions of 0- to 6- and 6- to 24-hr systems are generally quite similar to the all-event distribution. The number of 6- to 24-hr events is much less than the <6-hr events in most of the regions, except

10.1029/2019JD030449

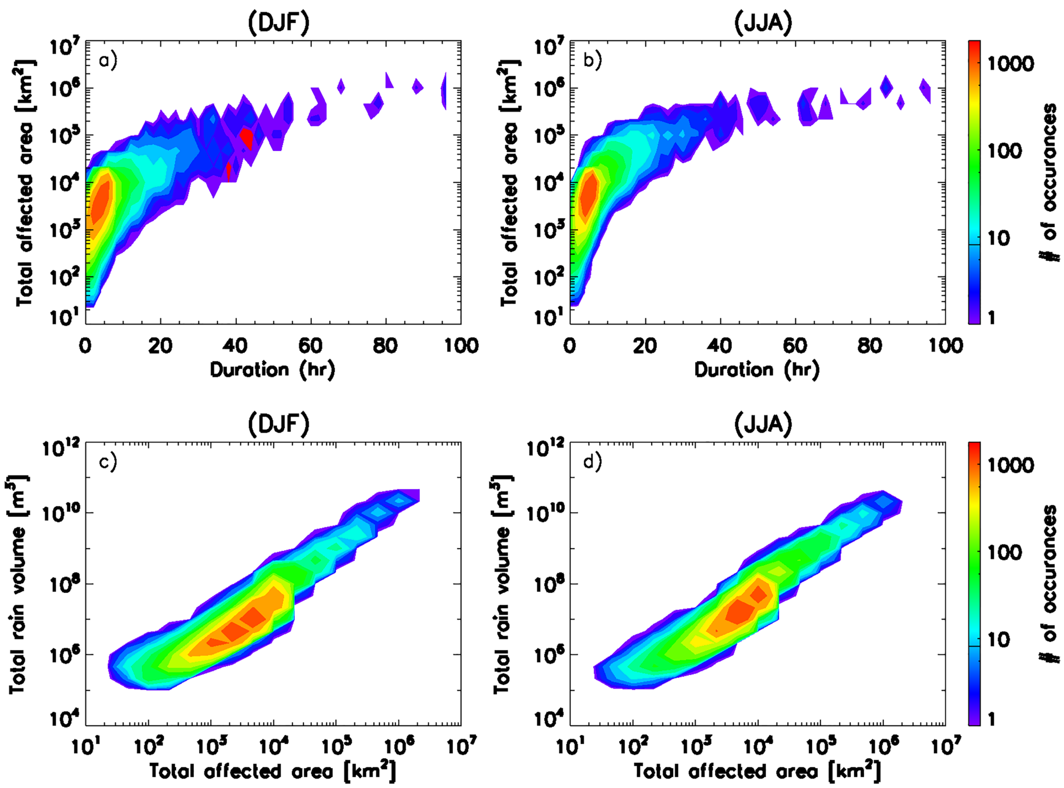

Figure 8. Histograms show relationships of duration with total affected area (upper panels) and total affected area with total rain volume (lower panels) for December–February (DJF; left) and June–August (JJA; right).

in the southeast and Florida Peninsula where 6- to 24-hr events outnumber the <6-hr events in summer and fall.

The frequency distributions of larger events, that is, total rain volume > 2.5×10^7 m^3 (Figures 7a–7d) and total affected area >7,000 km^2 (Figures 7e–7h), are quite similar to those of longer durations (Figures 6i–6l). The relationships between the total affected area, volume, and duration can be illustrated in two-dimensional histograms (Figure 8). Because the precipitation systems move, longer lived systems generally also have larger total affected areas, even though there is a large spread of total affected area for short duration events (Figures 8a and 8b). The relationship is nonlinear as the *x* axis for duration is linear and total area is exponential, and winter events have even larger spread in area for given duration than the summer events. The relationship between the total affected area and volume is better defined, even though 2 orders of spread in volume is observed for given area (Figures 8c and 8d). It is found that the majority of the storms have an affected area of 10^3–5×10^4 km^2 and volume of 10^6–10^8 m^3.

If the analysis is restricted to EPEs with maximum depths >12 mm, high concentration is found in regions along California's mountain ranges in cold seasons and southeast and Florida in JJA and SON, where intense precipitation is frequent, while eliminating many traveling winter events in the Midwest (Figures 7i–7l). Figure 7 illustrates how the flexibility in this database permits generating statistics based on different criteria for specific purposes.

3.2. Precipitation Duration, Start, End, and Peak Time

The temporal resolution of IMERG sets the duration of the shortest events to 30 min. Figure 9 shows the histograms of total duration of the EPEs (Figure 9a) and extreme duration, that is, the portion of events with extreme precipitation only (Figure 9b). As expected, the frequency of EPEs decreases approximately exponentially with increasing extreme duration (Figure 9b). The algorithm identifies many small events with just a few extreme precipitation grids both spatially and temporally that could be independent small events or disjoined cells of precipitation from a larger system that the algorithm fails to connect. The peak

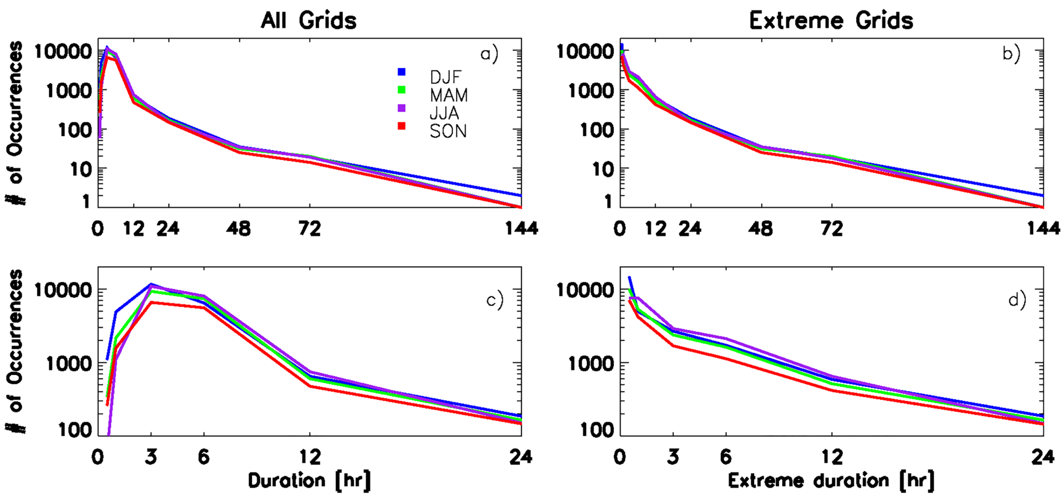

Figure 9. Frequency distributions of extreme events as a function of (a) duration computed from all grids for the entire event, and (b) extreme duration computed from extreme grids only for different seasons; (c) and (d) are subsets of (a) and (b), respectively, with duration of 0–24 hr. DJF = December–February; MAM = March–May; JJA = June–August; SON = September–November.

frequency of total duration of the events is between 3 and 6 hr. This is partly because light precipitation is allowed to extend 3 hr surrounding the extreme precipitating grids, making the total duration of events longer than the extreme portion of the events. JJA has slightly more events of all durations than the other seasons except for those that last fewer than 3 hr or more than 72 hr. DJF has the highest number of events with duration less than 3 hr and events that last more than 72 hr. The high number of multiday events in DJF is consistent with the usual understanding that winter has many precipitation systems that traverse CONUS for multiple days. SON has the least total number of events in all seasons. We found several events with duration longer than 288 hr (12 days) in each season. Again, there is a greater probability of those long events occurring in winter.

The diurnal cycle of EPEs can be represented by the starting and ending local times of each event (Figure 10). Shorter events (<6 hr) during JJA tend to begin between 11 A.M. and 4 P.M. local time and end between 3 and 4 P.M. or around 8 P.M. EPEs in MAM and SON show similar diurnal cycles, but the peak for both is much weaker than that in JJA. EPEs in DJF do not show any preference in event start and end time. The longer events (6–24 hr) start most frequently between 10 A.M. and 3 P.M. and end at 4 P.M. to 9 P.M. in the warm seasons. Multiday events appear to start and end randomly except for a slightly higher chance to start at around 1 P.M. in JJA.

A better indication of the diurnal cycle is to examine the change of precipitation volume during the day. We approximate this by looking at the frequency distribution of peak volume of the events with the local time (Figures 10c, 10f, and 10j). The result shows that peak volume occurs most frequently at 2–5 P.M. for <6-hr events and slightly later for 6- to 24-hr events. For multiday events, peak volume appears more prominently at 5–10 P.M. in JJA, around 8–10 P.M. in MAM and SON, near zero in the morning and gradually increasing after 12 P.M. in DJF. The peak volume distribution is more consistent with current understanding of summer time convection, which normally peaks at around 3–6 P.M. (Nesbitt & Zipser, 2003). Of course, one caveat of this analysis is the mixing of EPEs from different regions that might have different diurnal cycles, even though by stratifying with the seasons, the composition of events from each season has its preferred regions (Figures 6 and 7). The same caveat applies to the rest of analyses in this article.

3.3. Precipitation Depth and Intensity

Precipitation intensity at any single grid point can be measured by precipitation rate (precipitation per unit time) and/or depth. The intensity of the precipitation event as a whole can be measured by total precipitation area and volume at any given time.

Figure 11 shows the histogram of parameters that could indicate maximum storm intensity, including maximum precipitation rate (Figure 11a) and depth (Figure 11b) from a single grid point, system-wise maximum

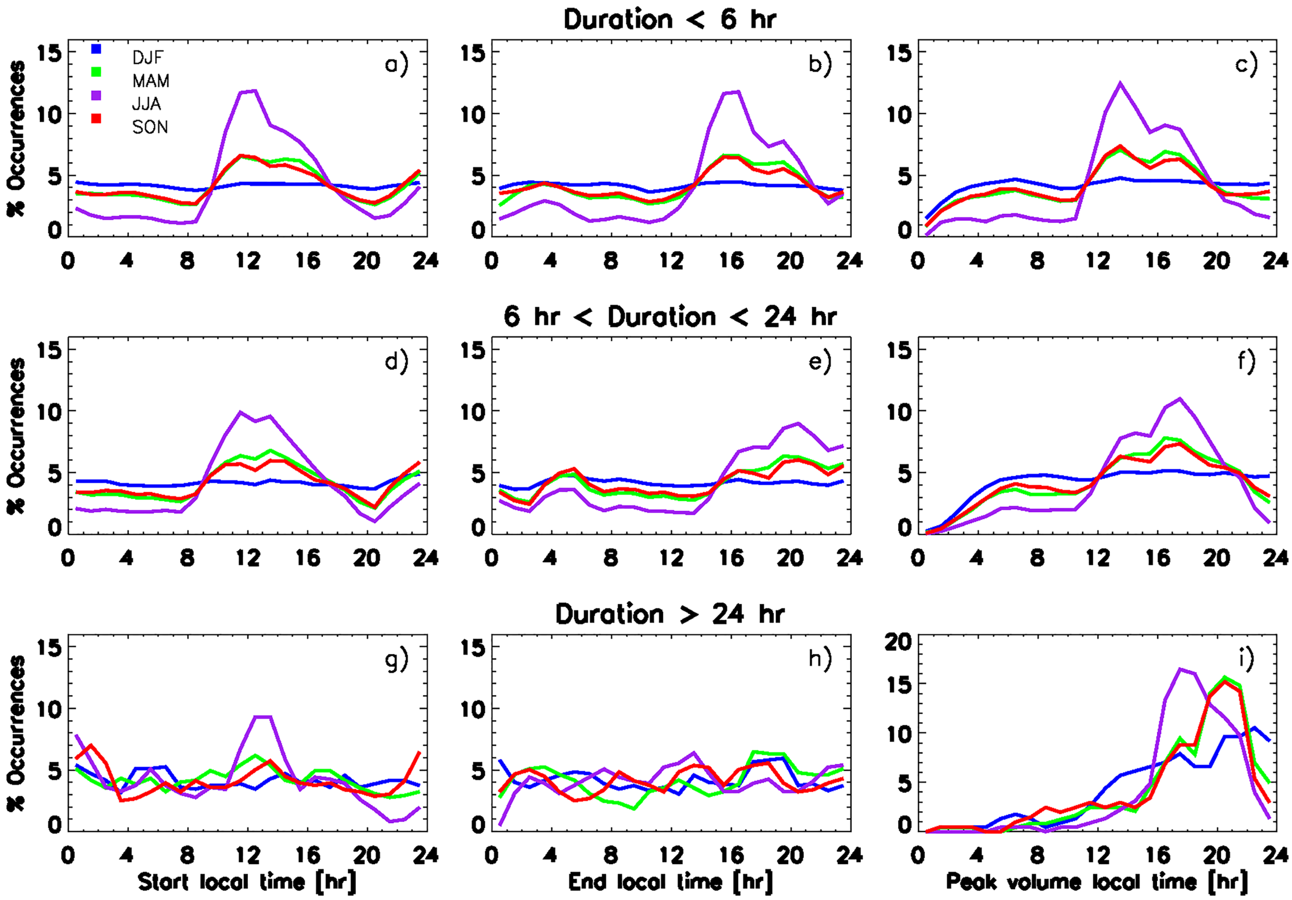

Figure 10. Frequency distributions of start, end, and at-peak volume local time for precipitation events with durations <6, 6–24, and >24 hr. Bin size is 1 hr. DJF = December–February; MAM = March–May; JJA = June–August; SON = September–November.

instantaneous total precipitating volume (Figure 11c) and size (area; Figure 11d), as well as the ratio of extreme precipitation versus total in volume (Figure 11e) and size (area; Figure 11f) during each event. These parameters are computed separately, so that they do not necessarily occur at the same time.

In Figure 11, there are two main peaks in the frequencies of maximum precipitation rate before an exponential decrease as precipitation rates increase. The first peak at 5 mm/hr should be considered primarily artificial, due to the minimum criterion in the event identification algorithm of 5 mm/hr for extreme precipitating grids and a requirement for each event to have at least one extreme precipitating grid. The second peak frequency is at about 10 mm/hr, with the summer season skewed slightly to the right and consistently higher precipitation rate (broad tail in the right). The maximum depth for the EPEs (Figure 11b) has a lower limit of 2.5 mm because each event contains at least one extreme precipitating grid. The peak frequency of maximum depth is around 10 mm in JJA and 5 mm in the other seasons. Summer also has a greater number of high single-grid accumulations (>20 mm) than the other seasons.

The maximum volume of a system (Figure 11c) is limited by the total water-holding capacity of the atmosphere and maximum moisture convergence at any instant. Figure 11c indicates that the JJA has more water-rich events than the other seasons. This is driven by the stronger moisture flux from warmer surrounding oceans and the Great Lakes in JJA (Figure 7c). Even though winter might have larger synoptic precipitation systems, apparently, a large portion of the precipitation area is not intense enough to be identified as extreme grids and the limited extension of events to light precipitation area (currently within 3 hr/6 km distance and greater than 1 mm/hr) have reduced its size. As a result, both maximum system size (Figure 11d) and the extreme-to-total size (Figure 11f) in DJF are smaller compared to the other seasons.

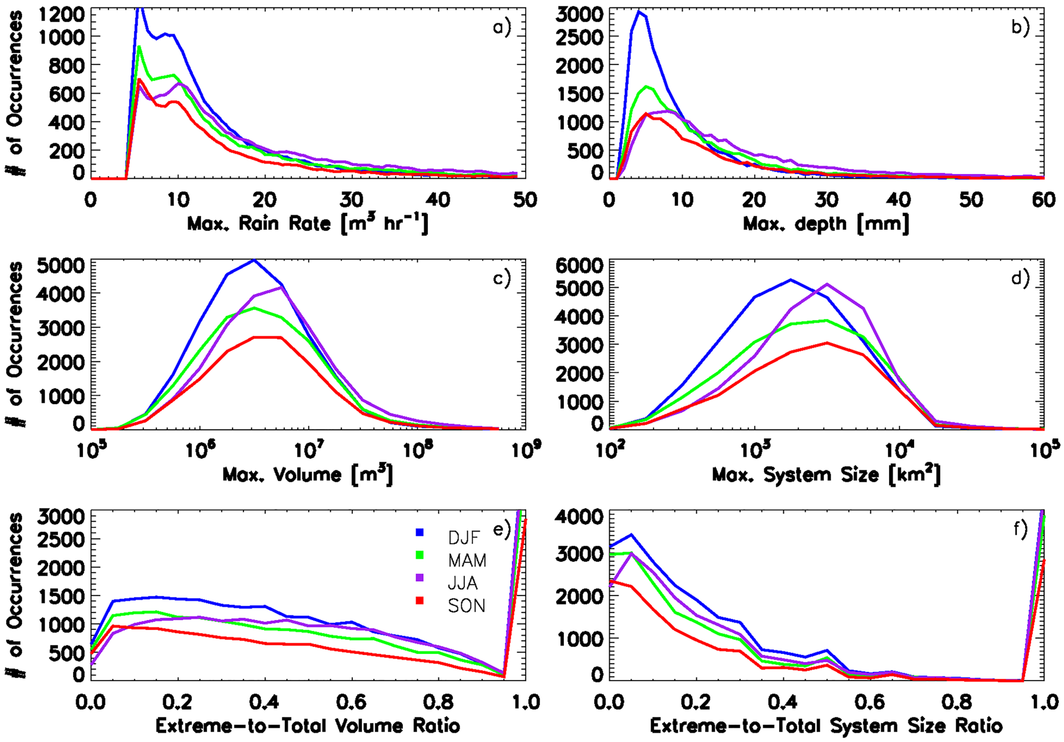

Figure 11. Instantaneous (half-hourly) properties of extreme events shown as frequency distributions of (a) maximum rain rate, (c) maximum half-hour rain volume, (d) maximum area coverage, (e) maximum extreme-to-total ratio of rain volume, and (f) maximum extreme-to-total ratio of rain size from different seasons over the entire domain. (b) Maximum depth is not instantaneous but a very localized property.

Extreme-to-total precipitation ratio (Figures 11e–11f) roughly indicates the ratio of convective versus total (convective plus stratiform) precipitation of the system, since convective precipitation tends to be heavier than the stratiform precipitation. The histograms of maximum extreme-to-total ratio shows a large number of systems with a maximum ratio of 1.0, indicating convective single-cell events. Otherwise, we observe that the volume ratio of extreme to total (Figure 11e) tends to be larger than the area ratio (Figure 11f). This is because the larger area of light precipitation does not contribute as much to the precipitation volume.

3.4. Total Volume and Affected Area

Previous studies have shown that the number of precipitation systems decreases exponentially when the sizes increase (Liu, 2011; Zhou et al., 2013). Figure 12 shows the histograms of a few parameters that characterize the entire event, including the mean precipitation rate, mean depth, total precipitation affected area, and total volumetric precipitation. These quantities are integrated from all precipitating grids from the entire system.

The mean precipitation rate from the extreme grids (Figure 12a) is much larger than that from the light precipitation grids (Figure 12b), as the former is set to be greater than 5 mm/hr, and light precipitation consists of those not identified as extreme precipitation (5 mm/hr or higher) but larger than 1.0 mm/hr. JJA has the most events with mean extreme precipitation rate greater than 10 mm/hr, followed by MAM and DJF. The SON has the smallest number of EPEs across all 4 years of data (Figure 12a). However, DJF has the highest mean light precipitation rates (Figure 12b) and mean precipitation rate (Figure 12c). This could be due to the artifacts of the light precipitation inclusion in the algorithm as mentioned in section 3.3. The limited extension to the light precipitation area has created more homogenous winter events where extremes are not as high and light not as low. The mean depth (Figure 12d) of the event is much smaller than the maximum depth (Figure 11b) because light precipitation contributes to a large percentage of the total affected area. The peak frequency for the mean depth is around 2 mm/hr for all the seasons except JJA, which has a greater number of extreme grids (Figure 12a). It is interesting to notice that even though the mean precipitation rate

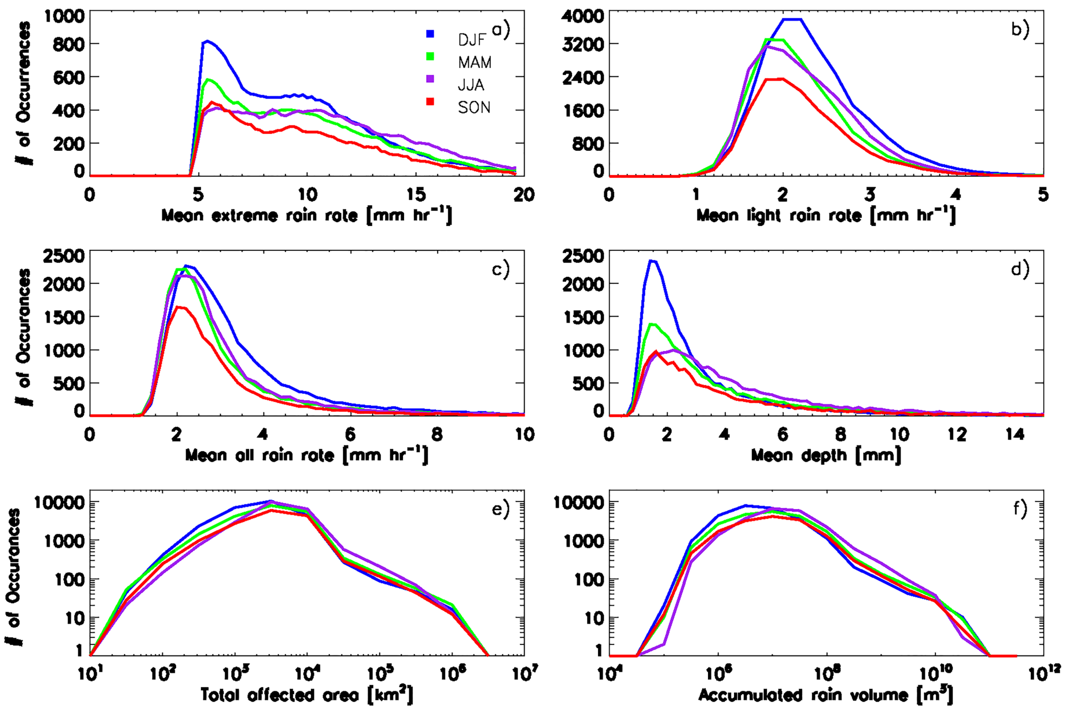

Figure 12. Frequency distributions of extreme event characteristics as a function of (a) mean extreme rain rate, (b) mean light rain rate, (c) mean all rain rate, (d) mean depth, (e) total affected area, and (f) accumulated rain volume. DJF = December–February; MAM = March–May; JJA = June–August; SON = September–November.

(Figure 12c) is higher in DJF than in JJA, JJA has higher mean depth (Figure 12d) because summer events are more stationary than the winter events, as will be shown later (Figure 13).

The total size of affected area (Figure 12e) and total precipitation volume (Figure 9f) are less skewed than the mean and maximum depth. The differences among the seasons appear to be smaller compared to the mean and maximum depth partly because of the logarithmic scales used. The peak frequency of total affected area occurs at 10^3–5×10^4 km^2 range (~90% of all events; Figure 12e), while the peak frequency of total volume occurs at 10^6–10^8 m^3 (~86% of total events; Figure 12f), consistent with what are shown in Figure 8. Summer has more than double the number of very wet events (total volume larger than 10^8 m^3) than the winter, that is, 3,183 versus1,479. This is because the frequency of summer MCS and thunderstorms in the southern United States outweighs the number of winter storms in the north (Figure 7).

3.5. Event Propagations

A unique aspect of EPEs that comes from this study's methodology is the capability to track the evolution of EPE both spatially and temporally. By locating the center of the event in each time step, we are able to track the propagation of events in both the zonal and meridional directions. Figure 13 shows the frequency distributions of the mean propagation speed stratified with duration and season. In the duration classes of <6 and 6–24 hr, about 20–40% of events have zero net speed, which are likely from stationary local convective events or stalled fronts, and are not included in the histograms. The percentage of stationary or near-stationary events is higher for short events (<6 hr) than the intermediate (6–24 hr) or longer events (>24 hr). Since the number of events with duration >24 hr is small, the histogram is rather noisy, but those events have the highest propagation speed (> 40 km/hr). The dependence of event propagation on duration is likely because shorter events are governed by their own life cycles, while longer events depend more on guiding large-scale synoptic circulations. The faster zonal speed compared to the meridional speed and faster winter and spring speed than summer and fall both indicate the dependence of precipitation propagation on large-scale circulation. This will provide a foundation to evaluate precipitation propagation under the warming climate as changes in large-scale circulation become more recognizable (Dwyer & O'Gorman, 2017).

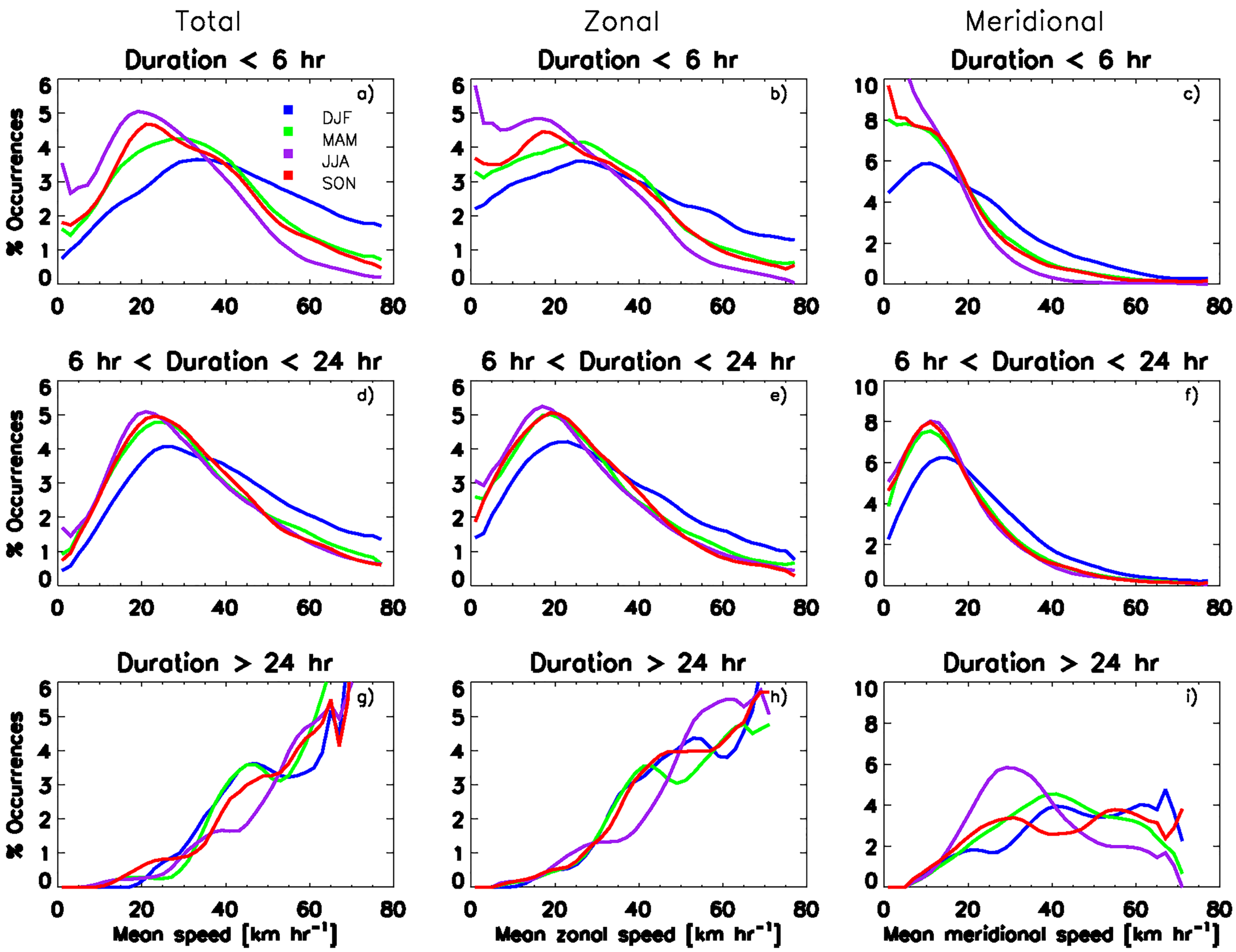

Figure 13. Mean event propagation speed (left column) and its zonal (middle column) and meridional (right column) components for events with duration of 0 < duration <6 hr (top row), 6 < duration <24 hr (middle row), and duration >24 hr (bottom row) events.

3.6. Subsetting the Database

As we learned from the above analyses, this EPE database includes EPEs from single extreme cells to events covering thousands of square kilometers. All the events belong to the tail distribution in some category in their specific locations. The parameters provided for each event makes it very easy to subset the types of events users want to study. For example, users interested in localized storms could set a requirement for high rain intensity and depth but relatively small size, likewise, users interested in larger events could require a larger size and total volume. It is also quite easy to eliminate unwanted events such as synoptic winter events and small breakout cells if the focus is on large convective events. For example, by requiring maximum depth of events to be greater than 20 mm and maximum instantaneous size greater than 1,000 km^2, the number of events will be reduced in 92.2% in winter and about 85%~72% in other seasons.

4. Summary and Discussion

Utilizing the high spatial and temporal resolution IMERG data, we constructed a database of EPEs that depicts both the spatial extent (*xy*) and temporal evolution (*t*) of precipitation systems. The EPEs were constructed using a recursive-fractal approach to organize the precipitating grids in space and time belonging to the same system into events, enabling accurate depiction of duration, areal coverage, total volume, and propagation of each EPE over its entire life cycle. The range of parameters provided for each event enable users to choose/subset the type of events they want to study as the database includes very different types of EPEs from single extreme cells to events that cover thousands of square kilometers.

We show detailed event statistics from 4 years of IMERG data derived over CONUS to illustrate the capabilities of this database. The spatial distributions of EPEs are consistent with seasonal precipitation distributions over CONUS, with winter and spring EPEs mostly occurring in the Northwest and Northeast, and summer EPEs in Southwest and Southeast. Fall has the smallest number of EPEs except near the coastal Pacific Northwest. The event parameters presented include event duration; start, end, and peak time; intensity and depth; maximum and total precipitation volume and areal coverage; and event propagation speed. We find the most frequent duration of EPEs to be 3–6 hr. The frequency decreases exponentially with duration afterwards. The diurnal cycle is most prominent in summer, weaker in spring and fall, and indiscernible in winter, especially for events lasting fewer than 6 hr. The mean and maximum precipitation intensity, size, and volume all show summer to be the season with the heaviest and largest precipitation events overall. The majority of the EPEs affect an area between 10^3–5×10^4 km^2 with total volume of 10^6–10^8 m^3. The event propagation speeds indicate the influence of large-scale circulation, as winter events tend to move faster than those in the other seasons.

The results from this study depend on the specific definition and subsequent algorithm of EPEs. Since many different types of extreme events exist from small intense thunderstorms to large monsoonal troughs, our algorithm is designed to encompass all these cases without being overly complicated. This inevitably leads to some caveats. First, we use a spatially varying but locally fixed extreme threshold to define the extreme grids. This allows the EPEs in each region to be specific in the context of its own climate, but a locally fixed threshold also means most of the EPEs will be concentrated in the wet seasons and it would be more difficult to monitor the changes in EPEs in the dry season. Second, the EPEs created in this study depend on a tunable searching distance and time interval in the algorithm. This is an intrinsically difficult problem as we tried to define an event. Whether separate cells of precipitation grids could be considered as a single event depends on system type and will inevitably depend on different regions and seasons. For example, synoptic winter systems usually move faster than summer organized convective systems, so a more relaxed interval may be needed to hold the system together. To use different criteria depending on system type may require other information, such as cloud or circulation fields. Doing so will make the algorithm considerably more complicated. However, even with fixed criteria, the current algorithm is able to capture major events without missing too much of total precipitation, meanwhile keeping the truly isolated events separate in their own right. In this regard, case studies of EPEs associated with Hurricane Harvey in 2017 and with atmospheric river events in the winter of 2015 demonstrate both the capability and limitation of the current algorithm.

The inherent uncertainties in IMERG data will also impact the precipitation intensity and coverage. The current IMERG product depends critically on the microwave estimates, meaning that over land, where this study concentrates, the retrievals depend on signals from solid hydrometeors. Thus, IMERG results are best when driven by typical, relatively deep precipitating systems. Potentially problematic areas include orographically driven or very tropical events in which warm rain enhancement (below the melting layer) is important and the retrievals (and hence IMERG) underestimate rates. In very dry regions and downwind of orography, evaporation in the lower reaches of precipitating systems eliminates small precipitation particles, leading the retrievals (and IMERG) to overestimate precipitation rates. When there is snow or ice on the surface, the retrievals currently used have difficulty detecting the solid hydrometeors aloft. At present, IMERG masks out the microwave estimates in such regions and uses infrared-based estimates, which tend to be much less certain. Finally, the morphing applied in IMERG between microwave overpasses tends to smooth out variations that occur on timescales shorter than the typical overpass interval, which is 2–3 hr. These uncertainties will affect the derived EPEs as well.

Ongoing work includes extending the database globally and for the entire TRMM-GPM period once the retrospective IMERG product becomes available, determining better extreme thresholds and spatial/temporal searching distance used in the algorithm. Additionally, we will examine the controlling mechanisms for different event characteristics. This EPE database will provide a wealth of information about precipitation events over different parts of the world, and the impact of climate forcings on event characteristics.

Appendix A: Derivation of Separate Set Variance/Standard Deviation for Extreme Events

Current computing limitations can make processing large data sets, and even large files, quite troublesome. In order to circumvent these computing and processing limitations, large data sets are often split up and processed in smaller subsets of the original data. In a serial computing environment, this works well for most functions and operations. For example, the mean of two equal-length vectors a and b can be described by

$$\frac{1}{n}\sum_{i=1}^{n} a_i + \frac{1}{n}\sum_{i=1}^{n} b_i = \frac{1}{n}\sum_{i=1}^{n} (a_i + b_i)$$

or in programming terms, MEAN(a) + MEAN(b) = MEAN(a + b). The mean of these two vectors is additive. However, some operations, like calculating the standard deviation, are not additive, and calculating the sum of the standard deviation of individual sets does not yield the same result as calculating the standard deviation over the whole data set. Because of our processing limitations, we have derived an approximation for the standard deviation calculated from multiple sets.

In our case, we can process about one month of data at a time. Let i be index of the month and j be the index of observations (precipitating grids, with $R > 0.01$ mm/hr) in any given month. Let M be the total number of month and N_i be the total number of observations in ith month. For any given month, we can easily compute the mean $\overline{x_i}$ and sum of square S_i of all precipitating grids and save these fields for later use.

$$\overline{x_i} = \frac{\sum_{j=1}^{N_i} x_{ij}}{N_i} \tag{1}$$

$$S_i = \sum_{j=1}^{N_i}\left[{x_{ij}}^2\right] \tag{2}$$

The variance equation for the entire data set is given as

$$V = \frac{\sum_{i=1}^{M}\sum_{j=1}^{N_i}\left(x_{ij} - Z\right)^2}{\sum\limits_{i=1}^{M} N_i} \tag{3}$$

$$Z = \frac{\sum_{i=1}^{M} N_i\overline{x_i}}{\sum_{i=1}^{M} N_i} \tag{4}$$

Here Z and V are the overall mean and variance, respectively. To derive V without prior knowledge of Z, we expand the above equation (3) as follows:

$$V' = \sum_{i=1}^{M}\sum_{j=1}^{N_i}\left(x_{ij} - z\right)^2 = \sum_{i=1}^{M}\sum_{j=1}^{N_i}\left(x_{ij}^2 - 2zx_{ij} + z^2\right)$$

Substituting and distributing the inner sum, we obtain

$$V' = \sum_{i=1}^{M}\left[S_i - 2z\left(N_i\overline{x_i}\right)\right] + N_{\mathrm{obs}}z^2 \tag{5}$$

Here, $N_{\mathrm{obs}} = \sum_{i=1}^{M} N_i$. All the terms required in (4) and (5) are precomputed in monthly files and thus manageable in terms of memory requirement. This procedure requires to read all the data only once thus makes processing efficient. Finally, we need to divide V' by the total number of observations less one so that

$$V = \frac{\sum_{i=1}^{M}\left[S_i - 2z\left(N_i\overline{x_i}\right)\right] + N_{\mathrm{obs}}z^2}{N_{\mathrm{obs}} - 1} \tag{6}$$

Using this formulation of variance, we can also calculate the standard deviation as

$$\sigma = \sqrt{V} \quad (7)$$

Acknowledgments
We thank two anonymous reviewers for many thoughtful comments of the initial version of this manuscript. The first author would like to thank Levon Demirdjian for discussion about the extreme event algorithm. Support from NASA NNH13ZDA001N-TERAQEA, NNH14ZDA001N-DSCOVR, and SCEX22019D is acknowledged. The IMERG data were downloaded from NASA GES DISC (https://doi.org/10.5067/GPM/IMERG/3B-HH/05). The extreme event statistics can be found in https://data.mendeley.com/datasets/r9d66gnvtm/draft?a = 0c85c966-b92c-4ba1-8597-3a1cad09ece9.

References

Agel, L., Barlow, M., Qian, J.-H., Colby, F., Douglas, E., & Eichler, T. (2015). Climatology of daily precipitation and extreme precipitation events in the northeast United States. *Journal of Hydrometeorology*, *16*(6), 2537–2557. https://doi.org/10.1175/JHM-D-14-0147.1

Allan, R. P., & Soden, B. J. (2008). Atmospheric warming and the amplification of precipitation extremes. *Science*, *321*(5895), 1481–1484. https://doi.org/10.1126/science.1160787

Atkins, N. T., & Wakimoto, R. M. (1997). Influence of the synoptic-scale flow on sea breezes observed during CaPE. *Monthly Weather Review*, *125*(9), 2112–2130. https://doi.org/10.1175/1520-0493(1997)125<2112:IOTSSF>2.0.CO;2

Blake, E. S., & Zelinsky, D. A. (2018). National Hurricane Center tropical cyclone report: Hurricane Harvey (AL092017).

Chang, W., Stein, M. L., Wang, J., Kotamarthi, V. R., & Moyer, E. J. (2016). Changes in spatiotemporal precipitation patterns in changing climate conditions. *Journal of Climate*, *29*(23), 8355–8376. https://doi.org/10.1175/JCLI-D-15-0844.1

Dairaku, K., Emori, S., & Oki, T. (2004). Rainfall amount, intensity, duration, and frequency relationships in the Mae Chaem watershed in Southeast Asia. *Journal of Hydrometeorology*, *5*, 458–470. https://doi.org/10.1175/1525-7541(2004)005<0458:RAIDAF>2.0.CO;2

Davis, C., Brown, B., & Bullock, R. (2006). Object-based verification of precipitation forecasts. Part I: Methodology and application to mesoscale rain areas. *Monthly Weather Review*, *134*(7), 1772–1784. https://doi.org/10.1175/MWR3145.1

Dias, J., Tulich, S. N., & Kiladis, G. N. (2012). An object-based approach to assessing the organization of tropical convection. *Journal of the Atmospheric Sciences*, *69*(8), 2488–2504. https://doi.org/10.1175/JAS-D-11-0293.1

Donat, M. G., Alexander, L. V., Yang, H., Durre, I., Vose, R., Dunn, R. J. H., et al. (2013). Updated analyses of temperature and precipitation extreme indices since the beginning of the twentieth century: The HadEX2 dataset. *Journal of Geophysical Research: Atmospheres*, *118*, 2098–2118. https://doi.org/10.1002/jgrd.50150

Donat, M. G., Lowry, A. L., Alexander, L. V., O'Gorman, P. A., & Maher, N. (2016). More extreme precipitation in the world's dry and wet regions. *Nature Climate Change*, *6*(5), 508–513. https://doi.org/10.1038/nclimate2941

Dwyer, J. G., & O'Gorman, P. A. (2017). Changing duration and spatial extent of midlatitude precipitation extremes across different climates. *Geophysical Research Letters*, *44*, 5863–5871. https://doi.org/10.1002/2017GL072855

Greve, P., Orlowsky, B., Mueller, B., Sheffield, J., Reichstein, M., & Seneviratne, S. I. (2014). Global assessment of trends in wetting and drying over land. *Nature Geoscience*, *7*(10), 716–721. https://doi.org/10.1038/ngeo2247

Groisman, P. Y., Knight, R. W., Easterling, D. R., Karl, T. R., Hegerl, G. C., & Razuvaev, V. N. (2005). Trends in intense precipitation in the climate record. *Journal of Climate*, *18*(9), 1326–1350. https://doi.org/10.1175/JCLI3339.1

Guan, B., & Waliser, D. E. (2015). Detection of atmospheric rivers: Evaluation and application of an algorithm for global studies. *Journal of Geophysical Research: Atmospheres*, *120*, 12,514–12,535. https://doi.org/10.1002/2015JD024257

Haerter, J. O., Berg, P., & Hagemann, S. (2010). Heavy rain intensity distributions on varying time scales and at different temperatures. *Journal of Geophysical Research*, *115*, D17102. https://doi.org/10.1029/2009JD013384

Hegerl, G. C., Zwiers, F. W., Stott, P. A., & Kharin, V. V. (2004). Detectability of anthropogenic changes in annual temperature and precipitation extremes. *Journal of Climate*, *17*(19), 3683–3700. https://doi.org/10.1175/1520-0442(2004)017<3683:DOACIA>2.0.CO;2

Higgins, R. W., Yao, Y., & Wang, X. -L. (1997). Influence of the North American monsoon system on the U.S. summer precipitation regime. *Journal of Climate*, *10*(10), 2600–2622. https://doi.org/10.1175/1520-0442(1997)010<2600:IOTNAM>2.0.CO;2

Huffman, G. J., Adler, R. F., Bolvin, D. T., & Nelkin, E. (2010). The TRMM Multi-satellite Precipitation Analysis (TMPA). In F. Hossain & M. Gebremichael (Eds.), *Satellite rainfall applications for surface hydrology* (pp. 3–22). Springer Verlag.

Huffman, G. J, Bolvin, D. T., Braithwaite, D., Hsu, K., Joyce, R., & Xie, P. (2018). NASA Global Precipitation Measurement Integrated Multi-satellitE Retrievals for GPM (IMERG), NASA Algorithm theoretical basis document (ATBD) version 5.2. (35 pp.). https://pmm.nasa.gov/sites/default/files/document_files/IMERG_ATBD_V5.2.pdf

Kendon, E. J., Roberts, N. M., Fowler, H. J., Roberts, M. J., Chan, S. C., & Senior, C. A. (2014). Heavier summer downpours with climate change revealed by weather forecast resolution model. *Nature Climate Change*, *4*(7), 570–576. https://doi.org/10.1038/nclimate2258

Konrad, C. E. II (1997). Synoptic-scale features associated with warm season heavy rainfall over the interior southeastern United States. *Weather and Forecasting*, *12*(3), 557–571. https://doi.org/10.1175/1520-0434(1997)012<0557:SSFAWW>2.0.CO;2

Kossin, J. P. (2018). A global slowdown of tropical cyclone translation speed. *Nature*, *558*(7708), 104–107. https://doi.org/10.1038/s41586-018-0158-3

Kunkel, K. E., Easterling, D. R., Kristovich, D. A. R., Gleason, B., Stoecker, L., & Smith, R. (2012). Meteorological causes of the secular variations in observed extreme precipitation events for the conterminous United States. *Journal of Hydrometeorology*, *13*(3), 1131–1141. https://doi.org/10.1175/JHM-D-11-0108.1

Lau, K.-M., Wu, H. T., & Kim, K. M. (2013). A canonical response of precipitation characteristics to global warming from CMIP5 models. *Geophysical Research Letters*, *40*, 3163–3169. https://doi.org/10.1002/grl.50420

Liu, C. (2011). Rainfall contributions from precipitation systems with different sizes, convective intensities, and durations over the tropics and subtropics. *Journal of Hydrometeorology*, *12*(3), 394–412. https://doi.org/10.1175/2010JHM1320.1

Liu, C., & Zipser, E. J. (2008). Diurnal cycles of precipitation, clouds, and lightning in the tropics from 9 years of TRMM observations. *Geophysical Research Letters*, *35*, L04819. https://doi.org/10.1029/2007GL032437

Liu, C., & Zipser, E. J. (2015). The global distribution of largest, deepest, and most intense precipitation systems. *Geophysical Research Letters*, *42*, 3591–3595. https://doi.org/10.1002/2015GL063776

Liu, C., Zipser, E. J., Cecil, D. J., Nesbitt, S. W., & Sherwood, S. (2008). A cloud and precipitation feature database from nine years of TRMM observations. *Journal of Applied Meteorology and Climatology*, *47*(10), 2712–2728. https://doi.org/10.1175/2008JAMC1890.1

Min, S. K., Zhang, X., Zwiers, F. W., & Hegerl, G. C. (2011). Human contribution to more-intense precipitation extremes. *Nature*, *470*(7334), 378–381. https://doi.org/10.1038/nature09763

Mock, C. J. (1996). Climatic controls and spatial variations of precipitation in the western United States. *Journal of Climate*, *9*(5), 1111–1125. https://doi.org/10.1175/1520-0442(1996)009<1111:CCASVO>2.0.CO;2

Mohr, K. I., Famiglietti, J. S., & Zipser, E. J. (1999). The contribution to tropical rainfall with respect to convective system type, size, and intensity estimated from the 85 GHz ice scattering signature. *Journal of Applied Meteorology*, *38*(5), 596–606. https://doi.org/10.1175/1520-0450(1999)038<0596:TCTTRW>2.0.CO;2

Nesbitt, S. W., Cifelli, R., & Rutledge, S. A. (2006). Storm morphology and rainfall characteristics of TRMM precipitation features. *Monthly Weather Review*, *134*(10), 2702–2721. https://doi.org/10.1175/MWR3200.1

Nesbitt, S. W., & Zipser, E. J. (2003). The diurnal cycle of rainfall and convective intensity according to three years of TRMM measurements. *Journal of Climate*, *16*(10), 1456–1475. https://doi.org/10.1175/1520-0442-16.10.1456

O'Gorman, P. A., & Schneider, T. (2009). The physical basis for increases in precipitation extremes in simulations of 21st-century climate change. *Proceedings of the National Academy of Sciences of the United States of America*, *106*(35), 14,773–14,777. https://doi.org/10.1073/pnas.0907610106

Pfahl, S., & Wernli, H. (2012). Quantifying the relevance of cy- clones for precipitation extremes. *Journal of Climate*, *25*(19), 6770–6780. https://doi.org/10.1175/JCLI-D-11-00705.1

Prein, A. F., Rasmussen, R. M., Ikeda, K., Liu, C., Clark, M. P., & Holland, G. J. (2017). The future intensification of hourly precipitation extremes. *Nature Climate Change*, *7*(1), 48–52. https://doi.org/10.1038/nclimate3168

Ren, F., Cui, D., Gong, Z., Wang, Y., Zou, X., Li, Y., et al. (2012). An objective identification technique for regional extreme events. *Journal of Climate*, *25*(20), 7015–7027. https://doi.org/10.1175/JCLI-D-11-00489.1

Schumacher, R. S., & Johnson, R. H. (2006). Characteristics of U.S. extreme rain events during 1999–2003. *Weather and Forecasting*, *21*, 69–85. https://doi.org/10.1175/waf900.1

Skok, G., Bacmeister, J., & Tribbia, J. (2013). Analysis of tropical cyclone precipitation using an object-based algorithm. *Journal of Climate*, *26*(8), 2563–2579. https://doi.org/10.1175/JCLI-D-12-00135.1

Skok, G., Tribbia, J., & Rakovec, J. (2010). Object-based analysis and verification of WRF model precipitation in the low- and midlatitude Pacific Ocean. *Monthly Weather Review*, *138*(12), 4561–4575. https://doi.org/10.1175/2010MWR3472.1

Skok, G., Tribbia, J., Rakovec, J., & Brown, B. (2009). Object-based analysis of satellite-derived precipitation systems over the low- and midlatitude Pacific Ocean. *Monthly Weather Review*, *137*(10), 3196–3218. https://doi.org/10.1175/2009MWR2900.1

Taylor, C. M., Belušić, D., Guichard, F., Parker, D. J., Vischel, T., Bock, O., et al. (2017). Frequency of extreme Sahelian storms tripled since 1982 in satellite observations. *Nature*, *544*(7651), 475–478. https://doi.org/10.1038/nature22069

Trenberth, K. E., & Zhang, Y. (2018). Near-global covariability of hourly precipitation in space and time. *Journal of Hydrometeorology*, *19*(4), 695–713. https://doi.org/10.1175/JHM-D-17-0238.1

Trenberth, K. E., Zhang, Y., & Gehne, M. (2017). Intermittency in precipitation: Duration, frequency, intensity, and amounts using hourly data. *Journal of Hydrometeorology*, *18*(5), 1393–1412. https://doi.org/10.1175/JHM-D-16-0263.1

Utsumi, N., Seto, S., Kanae, S., Maeda, E. E., & Oki, T. (2011). Does higher surface temperature intensify extreme precipitation? *Geophysical Research Letters*, *38*, L16708. https://doi.org/10.1029/2011GL048426

Vera, C., Higgins, W., Amador, J., Ambrizzi, T., Garreaud, R., Gochis, D., et al. (2006). Toward a unified view of the American monsoon systems, Published online on 15 October, 2006. https://doi.org/10.1175/JCLI3896.1

Wasko, C., & Sharma, A. (2015). Steeper temporal distribution of rain intensity at higher temperatures within Australian storms. *Nature Geoscience*, *8*(7), 527–529. https://doi.org/10.1038/ngeo2456

Westra, S., Fowler, H. J., Evans, J. P., Alexander, L. V., Berg, P., Johnson, F., et al. (2014). Future changes to the intensity and frequency of short-duration extreme precipitation. *Reviews of Geophysics*, *52*, 522–555. https://doi.org/10.1002/2014RG000464

White, R. H., Battisti, D. S., & Skok, G. (2017). Tracking precipitation events in time and space in gridded observational data. *Geophysical Research Letters*, *44*, 8637–8646. https://doi.org/10.1002/2017GL074011

Wu, X., Guo, S., Yin, J., Yang, G., Zhong, Y., & Liu, D. (2018). On the event-based extreme precipitation across China: Time distribution patterns, trends, and return levels. *Journal of Hydrology*, *562*, 305–317. https://doi.org/10.1016/j.jhydrol.2018.05.028

Zhang, X., Alexander, L., Hegerl, G. C., Jones, P., Klein Tank, A., Peterson, T. C., et al. (2011). Indices for monitoring changes in extremes based on daily temperature and precipitation data. *WIREs Climate Change*, *2*(6), 851–870. https://doi.org/10.1002/wcc.147

Zhou, Y., Lau, K. -M., & Liu, C. (2013). Rain characteristics and large-scale environments of precipitation objects with extreme rain volumes from TRMM observations. *Journal of Geophysical Research: Atmospheres*, *118*, 9673–9689. https://doi.org/10.1002/jgrd.50776

Zhou, Y., Lau, W. -K., Reale, O., & Rosenberg, R. (2010). AIRS Impact on precipitation analysis and forecast of tropical cyclones in a global data assimilation and forecasting system. *Geophysical Research Letters*, *37*, L02806. https://doi.org/10.1029/2009GL041494

Zwiers, F. W., & Kharin, V. V. (1998). Changes in the extremes of the climate simulated by CCC GCM2 under CO_2 doubling. *Journal of Climate*, *11*(9), 2200–2222. https://doi.org/10.1175/1520-0442(1998)011<2200:CITEOT>2.0.CO;2